

Propagation, cocoon formation, and resultant destabilization of relativistic jets

Jin Matsumoto¹  and Youhei Masada²

¹Research Institute of Stellar Explosive Phenomena, Fukuoka University, Fukuoka 814-0180, Japan

²Department of Science Education, Aichi University of Education, Kariya 448-8542, Japan

Accepted xxx, Received yyy, in original form zzz

ABSTRACT

A cocoon is a by-product of a propagating jet that results from shock heating at the jet head. Herein, considering simultaneous cocoon formation, we study the stability of relativistic jets propagating through the uniform ambient medium. Using a simple analytic argument, we demonstrate that independent from the jet launching condition, the effective inertia of the jet is larger than that of the cocoon when the fully relativistic jet oscillates radially owing to the pressure mismatch between jet and cocoon. In such situations, it is expected that the onset condition for the oscillation-induced Rayleigh–Taylor instability is satisfied at the jet interface, resulting in the destabilization of the relativistic jet during its propagation. We have quantitatively verified and confirmed our prior expectation by performing relativistic hydrodynamic simulations in three dimensions. The possible occurrences of the Richtmyer–Meshkov instability, oscillation-induced centrifugal instability and Kelvin–Helmholtz instability are also discussed.

Key words: galaxies: jets — instabilities — methods: numerical — relativistic processes — shock waves

1 INTRODUCTION

One of characteristic features of the astrophysical jet is its coherency in space and time. In contrast to that, it is implied from the recent studies that, in the relativistically-propagating jet, there exists small-scale disturbances, i.e., turbulence, which plays a considerable role in the particle acceleration and flaring activities of the jetted flow (e.g., [Asano & Terasawa 2015](#); [Asano & Hayashida 2015, 2018](#)). The large-scale coherency and small-scale incoherency, i.e., driven turbulence, are both fundamentally related to the nonlinear stability of the relativistic jet.

The evolution of the relativistic jet propagating through an ambient medium has been studied in high energy astrophysics. The dynamics and stability of jets from active galactic nuclei (AGNs) have been investigated through relativistic numerical simulations from 1990s ([Martí et al. 1997](#); [Gómez et al. 1997](#); [Komissarov & Falle 1997](#)). The propagation of the relativistic jet drilling a massive star is a key process in order to reveal the origin of the radiation mechanism for long gamma-ray bursts (GRBs; [Aloy et al. 2000](#); [Zhang et al. 2003](#); [Mizuta et al. 2006](#); [Morsony et al. 2007](#); [Lazzati et al. 2009](#); [Nagakura et al. 2011](#); [Ito et al. 2015, 2019](#); [Gottlieb et al. 2019](#)). The dynamics of a short GRB jet associated with a compact binary merger is a front line topic to understand electromagnetic counterparts to gravitational wave signals from the binary system ([Aloy et al. 2005](#); [Nagakura et al.](#)

[2014](#); [Murguia-Berthier et al. 2014](#); [Just et al. 2016](#); [Gottlieb et al. 2018a,b](#)). The stability of the propagating jet is crucial in order to maintain coherent structures of these relativistic jets.

On the other hand, relativistic jets are subjected to a storm of hydrodynamic (HD) and/or magnetohydrodynamic (MHD) instabilities when they propagate through the ambient medium. A velocity shear layer between the jet and surrounding medium is unstable to Kelvin–Helmholtz instability (KHI; [Turland & Scheuer 1976](#); [Blandford & Pringle 1976](#)). The observational structures, such as helices of jets, have been interpreted as the result of the growth of helical modes of the KHI. A helical motion of the jet itself leads to the deformation of the jet structure (e.g., [Aloy et al. 1999](#); [Perucho et al. 2019](#)).

The Poynting flux-dominated jets carrying large-scale helical magnetic fields can become unstable to current driven kink instability (CDI; [Lundquist 1951](#); [Spruit et al. 1997](#); [Begelman 1998](#)). The growth of the CDI is also the possible origin of the helical structure of the jet. In addition, the growth of the CDI may contribute to the energy conversion of the jet from the magnetic energy into the thermal energy via the magnetic reconnection ([Bromberg & Tchekhovskoy 2016](#)).

The rotation of the jet, which is the azimuthal component of the velocity against the jet axial velocity, is also a possible origin of the distortion of the jet interface. The rotational shears between the different jet components and/or surrounding medium can become unstable by the centrifugal-buoyancy force ([Meliani & Keppens 2007, 2009](#); [Millas et al. 2017](#)).

* E-mail: jin.matsumoto@fukuoka-u.ac.jp, jin@kustastro.kyoto-u.ac.jp

Even without the rotation of the jet, the centrifugal force can impact on the jet stability. [Gourgouliatos & Komissarov \(2018a\)](#) reported that the centrifugal instability (CFI) grew at the interface of AGN jets undergoing the reconfinement. This instability was responsible for the transition from the laminar to the turbulent flow at the reconfinement point and may be related to the physical origin of a morphological dichotomy of the AGN jets in the Fanaroff-Riley classification ([Fanaroff & Riley 1974](#)).

[Matsumoto & Masada \(2013, hereafter MM13\)](#) has shown other possible existence of the destabilization of the relativistic jet interface via oscillation-induced Rayleigh–Taylor instability (RTI) and associated Richtmyer–Meshkov instability (RMI) during jet propagation. Since they have non-axisymmetric nature, we had not captured them by conventional axisymmetric simulations of jet propagation (e.g., [Martí et al. 1997](#); [Gómez et al. 1997](#); [Komissarov & Falle 1997, 1998](#); [Scheck et al. 2002](#); [Mizuta et al. 2004](#); [Perucho & Martí 2007](#); [Meliani et al. 2008](#); [Mimica et al. 2009](#); [Mizuta et al. 2010](#); [Walq et al. 2013](#); [Mizuta & Ioka 2013](#); [Perucho et al. 2014](#)) while they may have been excited in three-dimensional (3D) simulations (e.g., [Aloy et al. 1999, 2003](#); [Hughes et al. 2002](#); [Zhang et al. 2004](#); [Rossi et al. 2008](#); [López-Cámara et al. 2013](#); [Li et al. 2018](#); [Gottlieb et al. 2018a,b, 2019](#); [Perucho et al. 2019](#)).

The physics of oscillation-induced RTI and RMI during jet propagation is summarized as follows (see MM13 for details): The radial inertia force, which is a main driver of the jet’s non-axisymmetric evolution, naturally arises when pressure mismatch exists between the jet and surrounding medium. Further, this force induces the radially oscillating motion of the jet and simultaneously excites the RTI at the interface between the jet and surrounding medium. Because the pressure mismatch is not alleviated immediately without some damping processes, it repeatedly excites the reconfinement shock inside the jet ([Sanders 1983](#); [Daly & Marscher 1988](#); [Matsumoto et al. 2012](#)). Then, RMI is additionally excited when the reconfinement shock collides with the jet interface and thus exhibits episodic growth with each collision (see, e.g., [Nishihara et al. 2010](#), for a review on RMI).

The linear theory of RTI at a discontinuous surface of relativistic flows is addressed in [Matsumoto et al. \(2017\)](#). The onset condition is given analytically by

$$\gamma_1^2 \rho_1 h_1' > \gamma_2^2 \rho_2 h_2', \quad (1)$$

where

$$h' := 1 + \frac{\Gamma^2 P_0}{\Gamma - 1 \rho c^2} \quad (2)$$

and the subscripts 1 and 2 represent the physical variables in the upper and lower region against the acceleration in the equilibrium state, respectively. Herein, γ is the Lorentz factor, ρ is the rest-mass density, Γ is the ratio of specific heats, c is the speed of light and P_0 is the interface pressure. This condition is applicable for analysing the stability of the interface among various jet components ([Toma et al. 2017](#)) and between the jet and surrounding medium. In the context of jet propagation, the onset condition (1) roughly indicates that the oscillation-induced RTI grows when the jet is effectively heavier than the surrounding medium.

When the jet is effectively lighter than the surroundings, the RTI is definitely stabilized by the negative buoyancy acting as the restoring force. It may be noteworthy that, in the situation where the RTI stable, the growth rates of instabilities accompanied by the radial displacement of the fluid parcel, such as CFI and KHI, would be more or less reduced by the negative buoyancy because it also acts against their destabilizing forces.

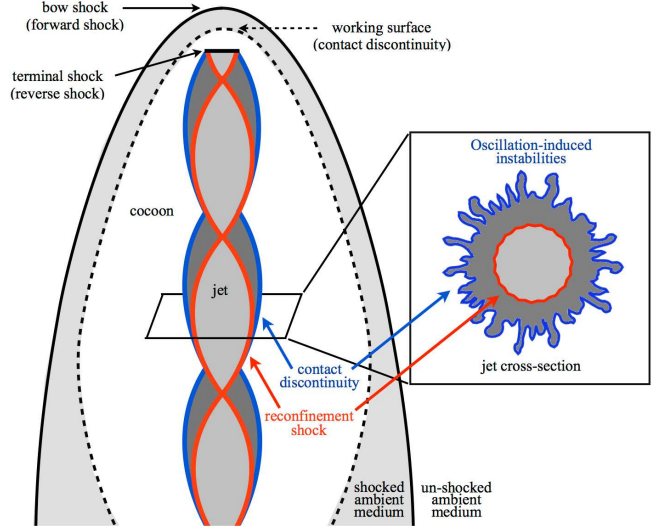


Figure 1. Schematic view of jet propagation through the ambient medium.

In this paper, we focus on the stability of the jet confined by a cocoon, as seen in the Fanaroff-Riley class II jet or the GRB jet drilling a progenitor star. Therefore, in the following, subscripts 1 and 2 in equation (1) correspond to jet and cocoon, respectively.

The cocoon is generated as a by-product of the jet propagation. When considering the propagation of a relativistic jet through the ambient medium, forward shock (bow shock), reverse shock (terminal shock) and contact discontinuity (working surface) are formed at the jet head. The matter that enters the jet head through forward or reverse shock is heated and separated by the working surface. The shocked jet matter forms a hot cocoon surrounding the jet itself. (See the schematic of the typical jet–cocoon–ambient medium system formed during the jet propagation shown in Fig. 1.) The physical condition of the cocoon should be dynamically determined by the jet propagation ([Begelman & Cioffi 1989](#); [Bromberg et al. 2011](#)) and thus cannot be understood without solving the interaction between the jet and ambient medium. Therefore, in the actual jet–cocoon system, it is unclear whether the onset condition for the oscillation-induced RTI is satisfied.

In this paper, in order to understand the basic physics of the growth of the oscillation-induced RTI and RMI in the jet, the non-linear stability of the relativistic jet propagating through the uniform ambient medium is addressed by taking account of the simultaneous cocoon formation. In Section 2, using a simple analytic argument, we demonstrate that the condition for the onset of RTI is possibly satisfied even in the realistic jet–cocoon system. In Section 3, we test and confirm the analytic prediction through 3D special relativistic hydrodynamic (SRHD) simulations. We discuss the possible development of instabilities in jets and the impact of the decaying pressure/density ambient medium and the magnetic field on the oscillation-induced RTI in Section 4. Finally, we summarize our findings in Section 5.

2 ANALYTIC PREDICTION ON STABILITY OF RELATIVISTIC JET INTERFACE

Generally, as described in Section 1, the jet is surrounded by the cocoon formed as a result of the shock heating at the jet head during

its propagation. It is thus expected that oscillation-induced RTI is excited at the jet interface when the onset condition (1) is satisfied between the jet and cocoon media. In this section, we demonstrate, with a simple analytic model, that the onset condition for the RTI is satisfied there as long as the jet is fully relativistic.

We suppose a situation where a relativistic flow is continuously injected into a homogeneous ambient medium. The effects of the magnetic field and rotation around the jet axis are ignored here. In such a situation, the shocked ambient medium, cocoon and jet regions are simultaneously formed inside the lobe of the forward shock as illustrated in Fig. 1. The gaseous medium consisting of each region is assumed to be uniform for the simplicity in the following.

The recurrence between overexpansion and overcontraction stages of the jet, which is induced by the pressure mismatch between the jet and cocoon, results in the radial oscillating motion of it. Then, time averagely, the pressure of the jet coincides with that of the cocoon due to the confinement of the jet by the cocoon. The internal energy and mass of the cocoon garnered through the reverse shock during the jet injection time, t , thus are estimated, when all the physical quantities characterizing the jet, such as jet radius, density, pressure, velocity, and Lorentz factor, are treated as the “temporally averaged” values, as follows:

$$\frac{P_c}{\Gamma - 1} V_c = \alpha \pi r_j^2 \gamma_j \rho_j c^2 (\gamma_j h_j - 1) (v_j - v_h) t, \quad (3)$$

$$M_c = \pi r_j^2 \gamma_j \rho_j (v_j - v_h) t \quad (4)$$

(Martí et al. 1997; Bromberg et al. 2011; Perucho et al. 2017), where subscripts j and c stand for the jet and cocoon respectively. Here, V_c is the volume of the cocoon, r_j is the jet radius, $h := 1 + \Gamma P / (\Gamma - 1) \rho c^2$ is the dimensionless specific enthalpy and v_h is the propagation velocity of the jet head. The parameter α is the conversion factor from the jet energy to the internal energy of the cocoon at the jet head. The other symbols retain the same meanings as those in Section 1.

It was reported from recent numerical studies of the propagation of AGN jets that roughly 40% of the jet energy is converted into the internal energy of the cocoon medium (Perucho et al. 2017). We thus choose the conversion factor as $\alpha = 0.4$ in the following.

From equations (3) and (4), the specific internal energy of the cocoon, ϵ_c , can be obtained as follows:

$$\frac{\epsilon_c}{c^2} = \frac{1}{\Gamma - 1} \frac{P_c}{\rho_c c^2} = \alpha (\gamma_j h_j - 1) = \alpha \left[\gamma_j \left(1 + \Gamma \frac{\epsilon_j}{c^2} \right) - 1 \right], \quad (5)$$

where $\rho_c = M_c / V_c$ is the rest-mass density of the cocoon and ϵ_j is the specific internal energy of the jet. The pressure of the jet “temporal-averagely” coincides with that of the cocoon as mentioned above. In addition, needless to say, there is no pressure jump across the interface between the jet and cocoon because the jet interface is regarded as a contact discontinuity. Therefore, the onset condition for the RTI (1) at the jet interface is rewritten, with equation (5), by

$$\gamma_j^2 \left(\frac{c^2}{\epsilon_j} + \Gamma^2 \right) > \left(\frac{c^2}{\epsilon_c} + \Gamma^2 \right) = \left(\frac{1}{\alpha (\gamma_j h_j - 1)} + \Gamma^2 \right). \quad (6)$$

Solving equation (6) numerically, we can find that the onset condition for the RTI is satisfied regardless of the magnitude of ϵ_j when $\gamma_j \gtrsim 1.2$ in cases $\Gamma = 4/3$ or $5/3$. Furthermore, when we suppose the relativistically hot jet ($\epsilon_j/c^2 \gg 1$ and $h_j \gg 1$) or cold jet ($\epsilon_j/c^2 \ll 1$ and $h_j \simeq 1$), the onset condition (6) reduces to

$$\gamma_j > 1. \quad (7)$$

This condition is always fulfilled in the jet. Therefore, overall our analysis predicts that the onset condition for the RTI at the interface between the jet and cocoon is satisfied when the jet propagates through the uniform ambient medium with a sufficient relativistic velocity ($\gamma \gtrsim 1.2$).

We verify the validity of our prediction in the next section. We discuss, in Section 4.2., the impact of the pressure/density stratification of the ambient medium, in which the ambient pressure decays with the jet propagation, on the growth of the RTI.

3 NUMERICAL VERIFICATION OF ANALYTIC PREDICTION

3.1 Numerical setup

To quantitatively confirm the analytic prediction presented above, we have conducted 3D SRHD simulations of the jet propagating through the uniform ambient medium in a cylindrical coordinate system (r, ϕ, z) . Assuming the ideal-gas law with the ratio of specific heats $\Gamma = 4/3$, the governing equations are

$$\frac{\partial}{\partial t} (\gamma \rho) + \nabla \cdot (\gamma \mathbf{v}) = 0, \quad (8)$$

$$\frac{\partial}{\partial t} (\gamma^2 \rho h \mathbf{v}) + \nabla \cdot (\gamma^2 \rho h \mathbf{v} \mathbf{v} + P \mathbf{I}) = 0, \quad (9)$$

$$\frac{\partial}{\partial t} (\gamma^2 \rho h c^2 - P) + \nabla \cdot (\gamma^2 \rho h c^2 \mathbf{v}) = 0, \quad (10)$$

where \mathbf{I} is the unit matrix and the other symbols maintain their previous meanings. Note that “ $\nabla \cdot$ ” denotes the divergence of variables in the cylindrical coordinates.

Additionally, we independently solve the advection of a passive tracer, which distinguishes the jet material ($f = 1$) from the ambient medium ($f = 0$), in conservation form:

$$\frac{\partial}{\partial t} (\gamma \rho f) + \nabla \cdot (\gamma \rho f \mathbf{v}) = 0. \quad (11)$$

A relativistic HLLC scheme (Mignone & Bodo 2005) is used to solve equations (8)–(11) in conservation form. The primitive variables are calculated from the conservative variables following the method of Mignone & McKinney (2007). We employ a MUSCL-type interpolation method to attain second-order accuracy in space, while second-order temporal accuracy is achieved using Runge-Kutta time integration. (See Matsumoto et al. 2012 and MM13 for details on our SRHD code.)

Initially, the calculation domain is filled with a homogeneous stationary ambient medium. A relativistic cylindrical jet with a radius of $r_{j,0}$ and aligned with the z -axis is continuously injected into the domain from the lower boundary at $z = 0$. The calculation domain spans $0 < r/r_{j,0} < 150$, $0 < \phi < 2\pi$ and $0 < z/r_{j,0} < 300$. The normalisation units in length, velocity, time and energy density are respectively selected as the jet radius at the injection point $r_{j,0}$, the speed of light c , the light crossing time over the jet radius $r_{j,0}/c$ and the rest-mass energy density in the ambient medium $\rho_a c^2$.

The grid spacing in the r -direction is grouped into two regions; an inner domain ($0 < r/r_{j,0} < 15$) and outer domain ($15 < r/r_{j,0} < 150$). We use a uniformly spaced grid consisting of 150 zones in the inner domain, whereas a geometrically stretched grid is adopted for the 40 zones of the outer domain. The injected jet is resolved by 10 numeric cells at the lower boundary and then, the main body of the jet is located within the inner domain during jet propagation for all our simulations. The polar angle of the calculation domain is uniformly divided into $\Delta\phi = \pi/80$. We also use a uniformly spaced

Table 1. List of simulation runs. The parameters are chosen so as the four models to be the representatives in parameter space of $h_j - \eta_{j,a}$.

Model	dominant energy	γ_j	$\rho_j c^2$	P_j	h_j	ϵ_j/c^2	$\eta_{j,a}$	L_j	$\rho_a c^2$	P_a
H-	internal	5	10^{-4}	10^{-3}	41	0.03	10^{-1}	$10^{-1}\pi$	1	10^{-4}
H+	internal	5	10^{-2}	10^{-1}	41	30	10^1	$10^1\pi$	1	10^{-2}
C-	kinetic	31	10^{-4}	10^{-6}	1.04	0.03	10^{-1}	$10^{-1}\pi$	1	10^{-7}
C+	kinetic	31	10^{-2}	10^{-4}	1.04	30	10^1	$10^1\pi$	1	10^{-5}

grid consisting of 3000 zones in the z -direction. The grid sizes for the r - and z - directions in the inner domain are same; $\Delta r/r_{j,0} = \Delta z/r_{j,0} = 0.1$. While a reflective boundary condition is imposed on the lower boundary outside the injection region of the jet ($r/r_{j,0} > 1$), an outflow (zero gradient) boundary condition is adopted for the outer boundary of the calculation domain.

The coordinate singularity is addressed by placing no grid point on the cylindrical axis and filling appropriate “ghost grids” in the region $r < 0$ (Mohseni & Colonius 2000; Ghosh et al. 2010). The physical variables are defined at the grid cell centre. The computational cell centre (r_i, ϕ_j, z_k) in the inner domain is defined as follows;

$$r_i = \left(i - \frac{1}{2}\right)\Delta r, \quad (i = 1, \dots, N_r), \quad (12)$$

$$\phi_j = \left(j - \frac{1}{2}\right)\Delta\phi, \quad (j = 1, \dots, N_\phi), \quad (13)$$

$$z_k = \left(k - \frac{1}{2}\right)\Delta z, \quad (k = 1, \dots, N_z), \quad (14)$$

where $(N_r, N_\phi, N_z) = (150, 160, 3000)$. The physical variables of the exterior ghost grid at (r_0, ϕ_j, z_k) are assigned to those of the interior grid at $(r_1, \phi_{j+N_\phi/2}, z_k)$ considering the sign as follows;

$$\mathbf{q}_{r_0, \phi_j, z_k} = \mathbf{q}_{r_1, \phi_{j+N_\phi/2}, z_k}, \quad (15)$$

$$\mathbf{q}'_{r_0, \phi_j, z_k} = -\mathbf{q}'_{r_1, \phi_{j+N_\phi/2}, z_k}, \quad (16)$$

where $\mathbf{q} = (\rho, P, v_z, f)$ and $\mathbf{q}' = (v_r, v_\phi)$. When we consider the second-order accuracy in space,

$$\mathbf{q}_{r_{-1}, \phi_j, z_k} = \mathbf{q}_{r_2, \phi_{j+N_\phi/2}, z_k}, \quad (17)$$

$$\mathbf{q}'_{r_{-1}, \phi_j, z_k} = -\mathbf{q}'_{r_2, \phi_{j+N_\phi/2}, z_k}. \quad (18)$$

When using the physical variables at the exterior ghost grids, we evaluate the numerical fluxes at the inner-most computational grids for the HLLC scheme.

3.2 Jet models

In this paper we focus on two parameters: relativistic hotness of the jet, h_j , and the effective inertia ratio of the jet to the ambient medium, $\eta_{j,a}$. Here, $\eta_{j,a}$ controls the morphology and dynamics of propagating jet and is given by a functional form as will be shown in what follows. Neglecting the multi-dimensional effect, the propagation velocity of the jet head through the ambient medium, v_h , can be evaluated by balancing the momentum flux of the jet and ambient medium in the frame of the jet head as follows:

$$v_h = \frac{\sqrt{\eta_{j,a}}}{1 + \sqrt{\eta_{j,a}}} v_j \quad (19)$$

(Martí et al. 1997; Mizuta et al. 2004). The relativistic internal energy and/or Lorentz factor of the fluid enhance the inertia. The ef-

fective inertia ratio, $\eta_{j,a}$, is thus obtained as

$$\eta_{j,a} = \frac{\gamma_j^2 \rho_j h_j}{\rho_a}. \quad (20)$$

Equation (19) indicates that the propagation velocity of the jet head, v_h , is roughly equal to the fluid velocity of the relativistic jet, v_j , in the regime where $\eta_{j,a} \gg 1$, while v_h is much slower than v_j and is not relativistic in the regime where $\eta_{j,a} \ll 1$.

Bearing in mind the confirmation of our prediction in various jet launching conditions, four-types of models, which are the representatives covering the parameter space of $\eta_{j,a}$ and h_j , are simulated. The parameters adapted in each model is summarized in Table 1. The relativistic hotness of the jet is distinguished by the labels “H” (hot with $h_j = 41$) or “C” (cold with $h_j = 1.04$). The relative inertia between jet and ambient medium is distinguished by the labels containing “+” (high relative inertia with $\eta_{j,a} = 10$) or “-” (low relative inertia with $\eta_{j,a} = 0.1$).

The relativistic hotness is related to the dominant type of energy in the jet. The specific internal energy is a good indicator for the dominant type of energy (e.g., Martí et al. 2016). The internal energy is dominant in the regime where $\epsilon/c^2 > 1$ while the kinetic energy is dominant in the regime where $\epsilon/c^2 < 1$. The relation between the relativistic hotness, h , and the specific internal energy, ϵ , is given by $h = 1 + \Gamma\epsilon/c^2$. The specific internal energy of the jet, ϵ_j/c^2 , in the hot and cold cases are 30 and 0.03, respectively. This indicates that hot and cold models in our simulations are classified as internal energy dominated and kinematically dominated, respectively.

The energy flux of the jet is defined by

$$L_j = \pi r_{j,0}^2 \gamma_j^2 \rho_j h_j c^2 v_j \sim \pi \eta_{j,a} r_{j,0}^2 \rho_a c^3. \quad (21)$$

Therefore, the jet power of the large inertia model (H+ and C+) is 10π while that of the small inertia model (H- and C-) is 0.1π . When we assume that the size of the jet radius at the nozzle is about 10 pc, the energy flux of the jet is estimated, for the case of the jet with small $\eta_{j,a}$, as follows;

$$L_j \sim 10^{44} \text{ erg/s} \times \left(\frac{r_{j,0}}{10 \text{ pc}}\right)^2 \left(\frac{\gamma_j}{5}\right)^2 \left(\frac{\rho_j/\rho_a}{10^{-4}}\right) \left(\frac{\rho_a}{1.4 \times 10^{-26} \text{ g/cm}^3}\right) \left(\frac{h_j}{41}\right) \quad (22)$$

where we chose ρ_a as the typical ambient density in the AGN system of 10^{-26} g/cm^3 . If we suppose the jet with large $\eta_{j,a}$, L_j is estimated as 10^{46} erg/s . In the case of a GRB jet propagating through a progenitor star with $r_{j,0} \sim 10^7 \text{ cm}$ and $\rho_a \sim 10^5 \text{ g/cm}^3$, L_j of small (large) inertia models are estimated as 10^{50} erg/s (10^{52} erg/s).

In our simulation models, the pressure ratio between the jet and ambient at the jet nozzle is set to be a relatively large value, i.e., $P_j/P_a = 10$. In this setting, the hot jet (models H- and H+) starts its evolution from the expansion stage, whereas the cold jet (models C- and C+) starts its evolution from the contraction stage because of the generation of the overpressured cocoon. If we change the initial pressure ratio, it does not have a significant impact on our results because the inertia ratio between the jet and ambient medium

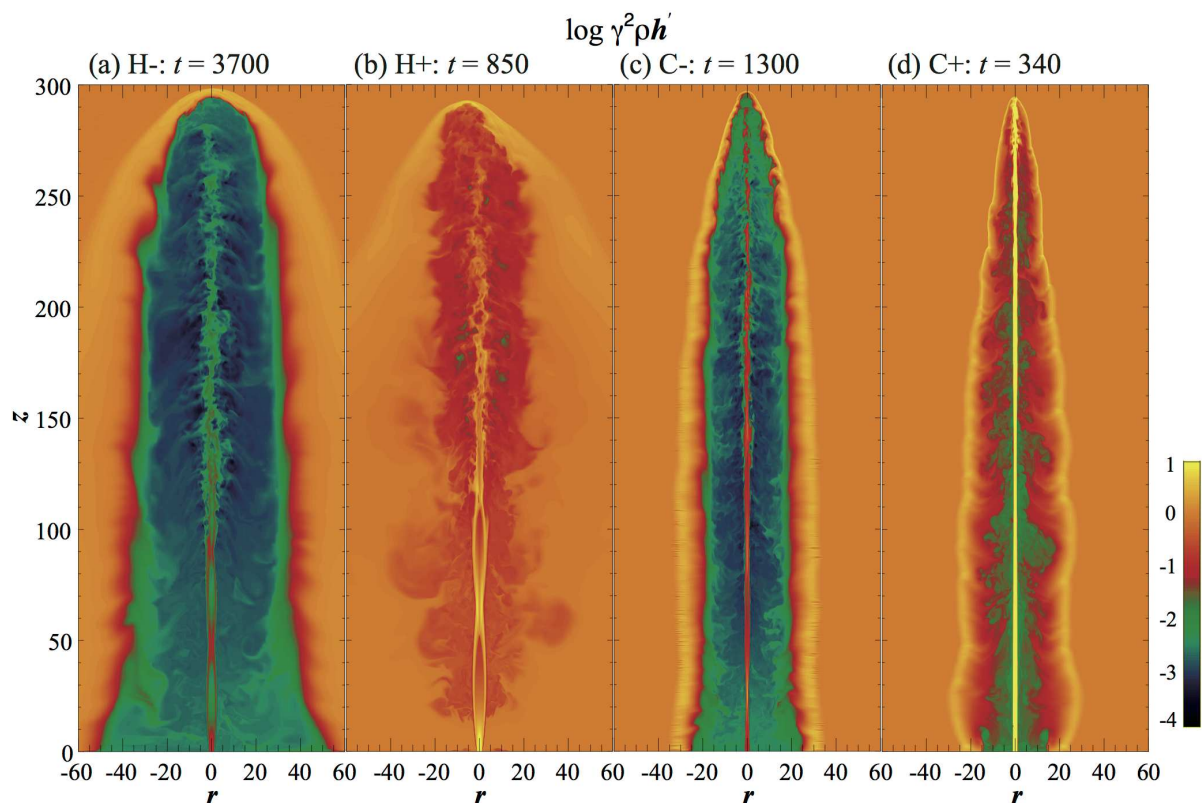


Figure 2. Spatial distribution of $\gamma^2 \rho h'$ on the cutting plane along the z -axis when the jet head reaches the upper boundary. Panels (a), (b), (c) and (d) correspond to the models H-, H+, C- and C+, respectively.

and the hotness of the jet which are the chosen key parameters in our simulations are mainly responsible for the morphology of the cocoon (Martí et al. 1997). Actually, recent 3D simulations of the AGN jet propagation reported that morphologies between the case with $P_j/P_a = 10$ and 1 were quite similar (Li et al. 2018).

A small-amplitude (1%) random pressure perturbation is introduced to the injected relativistic flow to break the symmetry of the jet as follows: White noise, $\delta(t, r, \phi, z)$, is generated at every time step for the pressure at the jet nozzle ($r < r_{j0}$ and $z < 0$). The maximum and minimum value of $\delta(t, r, \phi, z)$ are 0.01 and -0.01 , respectively. The pressure of the jet at the jet nozzle is given by $P_j(1 + \delta(t, r, \phi, z))$ as the boundary condition.

3.3 Confirmation of our analytic prediction

As can be observed, Fig. 2 presents a spatial distribution of $\gamma^2 \rho h'$, which is related to the onset condition for RTI, on the cutting plane along the z -axis at the final state of the simulation run (that is, when the jet head reaches the upper boundary at $z = 300$). Panels (a), (b), (c) and (d) in the figure correspond to models H-, H+, C- and C+, respectively. Note that the time of the final state ($= t_{\text{end}}$) differs owing to the propagation velocity of the jet among the four models, that is, $t_{\text{end}} = 3700$ (H-), 850 (H+), 1300 (C-) and 340 (C+).

The propagation velocity of the cold jet is typically faster than that of the hot jet when compared between models with the same η_{ja} . This result can be physically explained by the nonlinear dynamics of jet propagation. In the cold model, the pressure of the injected jet is generally smaller than that of the cocoon envelope because a large amount of the cold jet's kinetic energy is converted

into the thermal energy of the cocoon at the jet head. The initially-cold jet is thus compressed by the external cocoon's pressure as time advances and then gains the larger effective inertia than its hot counterpart. As a result, the propagation velocity increases more in the cold jet than in the hot jet at the same initial η_{ja} . The thickness of the cocoon envelope relative to the jet radius also varies among the four models. The slower the propagation velocity of the jet head, the thicker the cocoon envelope. These properties of the cocoon are common and well known in numerical simulations of jet propagation (e.g. Martí et al. 1997; Komissarov & Falle 1997).

As analytically predicted in Section 2, the $\gamma^2 \rho h'$ of the jet becomes larger than that in the cocoon envelope at the jet interface for all the models at the final state, regardless of the jet launching condition. Since the condition (1) is satisfied at the interface between the jet and cocoon, oscillation-induced RTI can grow there.

Fig. 3 presents the 3D rendering of the tracer in the range $f > 0.5$ for model H- when $t = 3700$. The rightmost depiction corresponds to the entire structure. The cross-sections at $z = 30, 65$ and 90 are also demonstrated for reference. The red tone denotes higher tracer value. Because the jet has a larger pressure compared to the cocoon, the jet expands radially around the jet nozzle, resulting in the excitation of reconfinement shock inside the jet. The distortion of the jet interface is clearly observed when the jet contracts radially (see the jet cross-section at $z = 30$ in Fig. 3). The growth of the oscillation-induced RTI is expected to contribute to the formation of the corrugated jet interface. The possible development of the other instabilities except RMI is discussed in Section 4.1.

The excited reconfinement shock inside jet converges to the jet

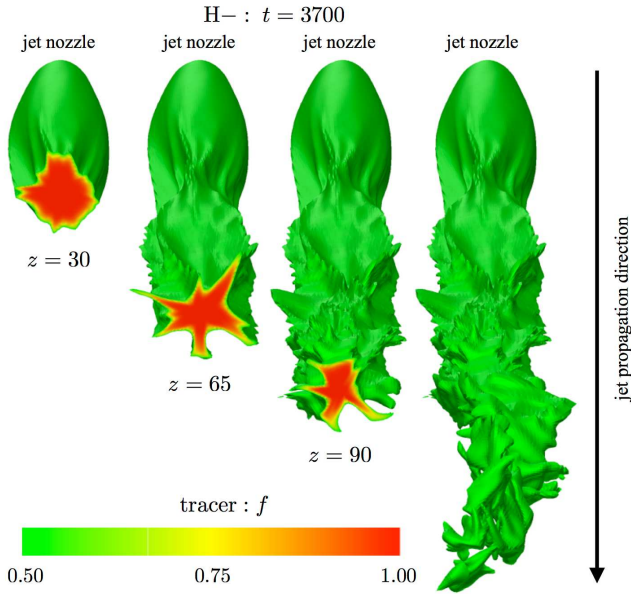


Figure 3. 3D rendering of the tracer (but only $f > 0.5$) at $t = 3700$ for model H-. The jet propagates from the top to bottom. The red tone denotes higher tracer value. Note that this plot is not linear in distance from the top to bottom because the viewing angle is chosen to exhibit the cross-section of the jet clearly.

axis and then transforms into radially outward propagating shock. When the outgoing shock encounters the contact discontinuity, RMI grows at the jet interface. Unlike oscillation-induced RTI, RMI grows impulsively when the reconfinement shock collides with the contact discontinuity (see Fig. 1 or MM13 for details on the excitation mechanism). The growth of the RMI secondary contributes to the amplification of the amplitude of the corrugated jet interface and the excitation of the elongated finger-like structures on the jet cross-section (Matsumoto & Masada 2013).

It is important to note that, in model H-, the first growth of RMI occurs around $z = 50$. Oscillation-induced RTI would be responsible for the distortion of the cross-section at $z = 30$. On the other hand, the elongated finger-like structures that appear in the cross-section at $z = 65$ and 90 result from the combination of oscillation-induced RTI and RMI.

Fig. 4 illustrates the 3D rendering of the tracer in the range of $f > 0.5$ for models H+, C- and C+ just after the jet head arrives at the upper boundary. The cross-section for each model is also pictured to clearly demonstrate the deformed jet interface. The viewing angle is chosen to suit each model respectively. In all three models, the elongated finger-like structures are also excited on the jet cross-section with the radially oscillating motion. Although the relativistic jet demonstrates a rich variety of propagation dynamics depending on the launching conditions, the oscillation-induced RTI and associated RMI could grow mutually at the jet interface, inducing a significant number of finger-like structures. Overall, the simulation results confirm our analytic prediction and suggest that the deformation of the relativistic jet interface is unavoidable in a purely hydrodynamic regime unless some constricting effects exist on the radial oscillating motion of the jet. The possible effects of the suppression of the growth of the oscillation-induced RTI are discussed in the following section.

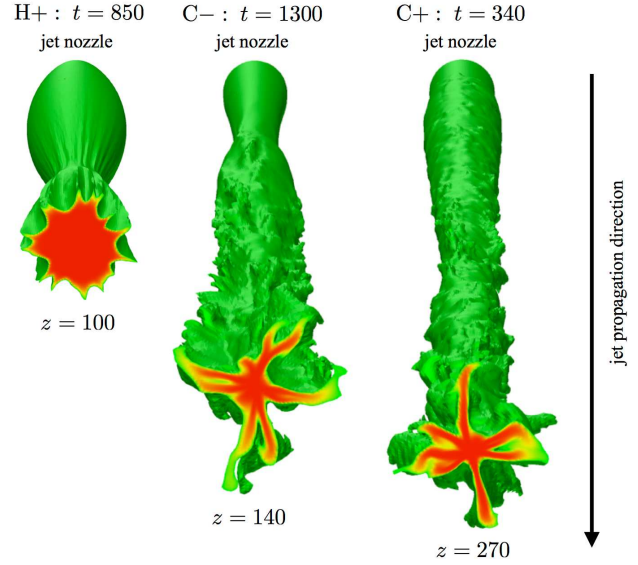


Figure 4. 3D rendering of the tracer (but only $f > 0.5$) for models H+, C- and C+ when the jet head reaches the upper boundary ($z = 300$). Color means the same as Figure 3. The red tone denotes higher tracer value. Jets propagate from the top to bottom. The viewing angle is chosen to be suited for each model.

4 DISCUSSION

4.1 Possible development of instabilities in jets

Because the effects of the magnetic field and rotation (i.e., the bulk azimuthal velocity) of jets are ignored in this work for simplicity, the growth of the CDI and rotation-induced instability (Meliani & Keppens 2007, 2009; Millas et al. 2017) is not expected in this study.

The development of the KHI in relativistic jets has been investigated diligently (e.g. Turland & Scheuer 1976; Blandford & Pringle 1976; Ferrari et al. 1978; Hardee 1979; Hardee et al. 1998, 2001; Perucho et al. 2004, 2005, 2007; Mizuno et al. 2007; Rossi et al. 2008; Perucho et al. 2010). From the stability analysis of jets to the KHI, it is widely known that, in the case the radial oscillating motion of the jet is absent, the reflection body mode becomes dominant when the flow velocity of a jet is supersonic (e.g., Payne & Cohn 1985; Perucho et al. 2004, 2010). This mode invokes the small-scale disturbance of the jet interface while the surface mode contributes to the global-scale deformation of the jet. Therefore, even in our models, the body mode of the KHI may play a role in generating the small-scale disturbances at the jet interface.

Not only the RTI and RMI, CFI should develop as well when the jet has radial oscillating motion (Gourgouliatos & Komissarov 2018a,b). The jet moves along curved streamlines with relativistic velocity at the radially oscillating interface of the jet (blue lines in Fig. 1), where the centrifugal force essentially balances the pressure gradient force of the jet. However, the cocoon does not move fast at the jet interface compared to the jet. Therefore, the angular velocity along the curved streamlines jumps across the jet interface and drastically decreases from the jet towards the cocoon. The onset condition for the growth of CFI is thus expected to be satisfied in this situation (see, Gourgouliatos & Komissarov 2018a, for details).

Since the inertia force, which induces the oscillation motion of

the jet, is responsible for both the RTI and CFI, the typical growth time of these instabilities is expected to be compatible with the oscillation time-scale of the jet, τ_{osci} . Qualitatively, the τ_{osci} can be estimated as the free-fall time of the jet radius, that is $\tau_{\text{osci}} \sim \sqrt{r_j/g}$ where r_j is the jet radius and g is an effective acceleration. In the case of the RTI, above speculation is consistent with the linear theory (Matsumoto et al. 2017). The typical linear growth time of the RTI is given by $\tau_{\text{RTI}} \sim 1/\sqrt{gk}$ where k is the wavenumber. When taking $k \sim 1/r_j$, we can find that τ_{RTI} coincides with τ_{osci} .

Since the origin of oscillation-induced instabilities is the same and no difference in the growth rate of the instabilities is expected, it is difficult to distinguish the RTI and CFI at a glance. However, it is obvious that only the CFI grows at the jet interface in the case where the jet is surrounded by a dense medium compared to the jet (Gourgouliatos & Komissarov 2018a) because the jet is RTI stable in such a situation.

As described in the introduction, the non-axisymmetric modes of the RTI and RMI cannot be excited in conventional axisymmetric simulations of jet propagation. In order to confirm it, 2D counterparts for all the four models are simulated in the cylindrical coordinate system with the same resolutions as 3D models, that is, $\Delta r/r_{j,0} = \Delta z/r_{j,0} = 0.1$. Fig. 5 shows the density distribution of 2D counterparts. As expected, we can find that the jet can propagate stably under the constraint of the axisymmetry. The results of these 2D counterparts indicate that the non-axisymmetric modes of some instabilities are responsible for the destabilization of the jet in our 3D simulations although it is still difficult to identify the main player. It would be a challenge for our future work to identify the dominant instability mode.

4.2 A simple relationship between hotness and velocity of the jet and its stability

A simple scaling relation between the hotness and velocity of the jet and its stability to the RTI can be obtained from a qualitative argument. The inertia force, which induces the radially oscillating motion of the jet, balances with the pressure gradient force of the jet:

$$\gamma_j^2 \rho_j h_j g = -\nabla P_j. \quad (23)$$

This relation provides a rough estimation of the acceleration g as

$$g \sim \frac{c_{s,j}^2}{\gamma_j^2 r_j}, \quad (24)$$

where $c_{s,j}$ is the sound speed of the jet. Therefore, the growth rate of the oscillation-induced RTI, σ , has the following relation;

$$\sigma \sim \frac{1}{\tau_{\text{osci}}} \propto \sqrt{\frac{g}{r_j}} \sim \frac{c_{s,j}}{\gamma_j r_j} \sim \frac{v_j}{\gamma_{s,j} r_j M_{\text{rela},j}}, \quad (25)$$

where $M_{\text{rela},j} = \gamma_j v_j / \gamma_{s,j} c_{s,j}$ is the relativistic Mach number of the jet (Konigl 1980; Komissarov & Falle 1998) and $\gamma_{s,j}$ is the Lorentz factor of the jets sound speed. This indicates that the hotter jet is more unstable to the RTI than the colder jet because the growth rate of it is proportional to the sound speed of the jet. In addition, the faster (higher relativistic Mach number and/or Lorentz factor) jet becomes more stable to the RTI. These tendencies of the jet stability to the RTI in the linear regime are similar to those to the KHI (Perucho et al. 2010) and are observable even in our simulations when comparing the jet stability between the models with the same inertia. Hot jets lose their coherent shapes violently compared to their cold and faster counterparts as shown in Fig. 2.

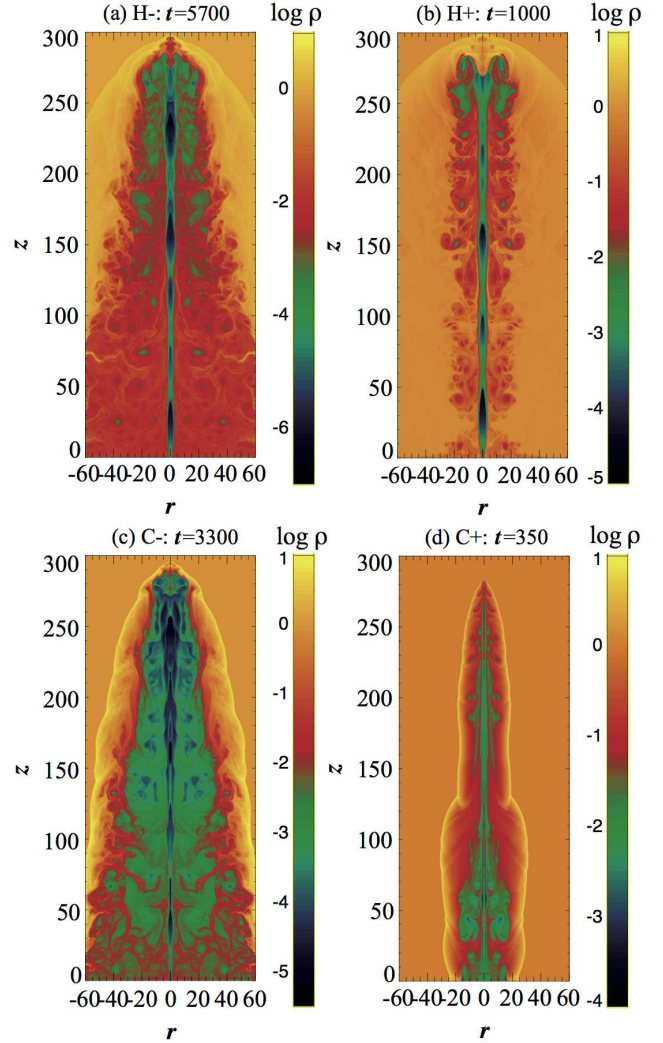


Figure 5. Density distribution of 2D axisymmetric simulations for four models (H-, H+, C- and C+).

4.3 Jet propagation through decaying pressure medium

In the actual astrophysical system, the jet propagates through an inhomogeneous medium where the density and pressure drop with the propagation (e.g., Perucho & Martí 2007; Perucho et al. 2011). Then, the thermodynamical properties of the cocoon are expected to change with time. Since the physical properties, such as the typical growing scale, of oscillation-induced instabilities are associated with the reconfinement of the jet by the cocoon, a change of the propagation environment should impact on the stability of the jet.

The reconfinement region and thus the jet radius become large with time when the jet propagates through the ambient gas with a decaying density and pressure profiles (e.g., Matsumoto et al. 2012). In such a situation, the growth rate of the oscillation-induced instabilities becomes small compared to the case where the jet propagates through the uniform ambient medium. The larger jet radius provides the longer oscillation time. This would be the reason for it. We note that the rough estimation of the growth rate of the oscillation-induced RTI (25) also predicts such a behavior of the jet though it is derived from the local balancing of forces.

We finally stress that, when the ambient density and pressure decrease drastically and the jet enters into the free expansion

sion phase, the jet becomes stable to the oscillation-induced instabilities because in such a situation, the reconfinement process no longer works, resulting in a loss of causal connectivity across the jet (Porth & Komissarov 2015).

4.4 Effect of magnetic field

The magnetic field plays a variety of roles in the propagation of relativistic jets (e.g., Komissarov 1999; Leismann et al. 2005; Bromberg et al. 2014; Mizuno et al. 2015; Martí et al. 2016). The toroidal component of it pinches the jet and weakens the inward motion of the rarefaction waves, resulting in the formation of weaker reconfinement shocks and rarefaction waves than those in a purely HD jet. On the other hand, since the axial component of it gives rise to a magnetic pressure additional to the gas pressure, it leads to stronger reconfinement shocks and rarefactions.

The toroidal magnetic field is expected to be dominant in the jet at the larger distance from the jet formation region (Baum et al. 1997; Laing & Bridle 2014). When considering a strong-ordered magnetic field, the magnetic tension force due to the toroidal field would more or less contribute to the suppression of non-axisymmetric modes of the oscillation-induced RTI which have the wavevector parallel to the direction of the magnetic field.

In the non-relativistic regime, when the wavevector, \mathbf{k} , is parallel to the magnetic field, \mathbf{B} , the growth rate of the magnetic RTI is given by

$$\omega^2 = -gk \left[A - \frac{B^2 k}{2\pi(\rho_+ + \rho_-)g} \right], \quad (26)$$

where ρ_+ and ρ_- are the upper and lower density against an acceleration, g , respectively, and $A = (\rho_+ - \rho_-)/(\rho_+ + \rho_-)$ is the Atwood number (Chandrasekhar 1961; Hillier 2016). At the limit $B = 0$, this reduces to the growth rate of the RTI for purely hydrodynamic case;

$$\omega^2 = -gkA. \quad (27)$$

The critical wavelength λ_c is obtained from above dispersion relation for the magnetic RTI as

$$\lambda_c = \frac{B^2}{(\rho_+ - \rho_-)g}. \quad (28)$$

The strength of the magnetic field characterizes λ_c and the RTI mode with $\lambda < \lambda_c$ is then suppressed due to the magnetic tension force.

Next, the magnetic RTI in the relativistic regime is in our interest. However, it is not sufficiently investigated even at the linear stage. Here we speculate the linear property of the relativistic magnetic RTI in analogy with its non-relativistic counterpart.

The growth rate of the relativistic RTI for purely hydrodynamic case is given by

$$\omega^2 = -gk\mathcal{A}, \quad (29)$$

where \mathcal{A} is the relativistic Atwood number (Matsumoto et al. 2017). Based on this, the growth rate and the critical wavelength of the “relativistic” magnetic RTI in the jet–cocoon system are surmised as follows: The density in equations (26) and (28) would be replaced, physically and intuitively, by the effective inertia in the relativistic regime. Based on the dispersion relation for the relativistic hydrodynamic RTI (29), the Atwood number in equation (26) should be replaced by the relativistic Atwood number as well.

Then, the growth rate and critical wavelength of the relativistic magnetic RTI at the jet interface are expected to be

$$\omega^2 \sim -gk \left[\mathcal{A} - \frac{B^2 k}{2\pi(\gamma_j^2 \rho_j h_j + \gamma_c^2 \rho_c h_c)g} \right], \quad (30)$$

and

$$\lambda_c \sim \frac{B^2}{(\gamma_j^2 \rho_j h_j - \gamma_c^2 \rho_c h_c)g}, \quad (31)$$

respectively.

When the inertia of the jet is much larger than the cocoon, the RTI grows faster. Even in the limit where $\gamma_j^2 \rho_j h_j \gg \gamma_c^2 \rho_c h_c$, the critical wavelength is not vanished and continues to exist. In such a situation, when considering the balance between the pressure gradient force and inertia force at the jet interface, the typical wavelength of the magnetic RTI is given, with the similar procedure as Section 4.2, by

$$\lambda_c \sim \frac{8\pi r_j}{\beta}, \quad (32)$$

where $\beta = P_j/(B^2/8\pi)$ is the plasma beta. Since the diameter of the jet cross-section is given by $2\pi r_j$, all the modes of the RTI potentially excited in the jet would be suppressed if β is the order of or smaller than unity.

Not only the RTI, the magnetic field also gives various impacts on the instabilities and their resultant in the jet. For example, Komissarov et al. (2019) show recently that the magnetic tension force due to the toroidal field contributes to the suppression of the oscillation-induced CFI if the strength of it is greater than a certain level. When the strength of the magnetic field is weaker, the oscillation-induced instabilities are expected to amplify the magnetic field via small-scale turbulent dynamo.

In contrast, there exists a case that the magnetic field itself becomes unstable. When the jet is strongly dominated by the azimuthal magnetic component, it is well known that the jet becomes unstable to CDI (e.g., Eichler 1993; Mizuno et al. 2009; Porth & Komissarov 2015). Overall the impact of the magnetic field on the jet propagation dynamics is still controversial because it is deeply related to the origin of it, in other word, the central engine of the jet. It is not fully explored and within the scope of our future work.

5 SUMMARY

The nonlinear stability of relativistic jets propagating through the uniform ambient medium was studied analytically and numerically by considering the simultaneous formation of cocoons. Our analytic findings indicate that the onset condition for oscillation-induced RTI is satisfied at the interface between a fully relativistic jet and its cocoon, regardless of launching conditions when the jet oscillates radially. To verify this prior expectation, we performed 3D SRHD simulations of a relativistic jet propagating through the homogeneous ambient medium. Based on the parameters studied with two varying fundamental jet launching conditions (hotness of the jet and effective inertia ratio between the jet and ambient medium), we confirmed that oscillation-induced RTI also grows at the relativistic jet interface in addition to RMI, oscillation-induced CFI and KHI. Hence, we can conclude that the synergetic growth of these instabilities at the jet interface is an inherent property of relativistic hydrodynamic jets propagating through the uniform medium.

To correctly capture HD and MHD instabilities and obtain the whole picture of a relativistic jet in its actual astrophysical environment, high-resolution 3D MHD modelling is required. We have attempted the first step towards fully understanding astrophysical relativistic jets in this study.

ACKNOWLEDGEMENTS

We thank H. R. Takahashi, A. Mizuta, S. Nagataki, M. A. Aloy, J. M. Martí, M. Perucho, S. S. Komissarov and K. N. Gourgouliatos for their useful discussions. Numerical computations were conducted on Cray XC30 at the Center for Computational Astrophysics, National Astronomical Observatory of Japan and on Cray XC40 at YITP at Kyoto University. This work was supported in part by Research Institute of Stellar Explosive Phenomena at Fukuoka University and the Center for the Promotion of Integrated Sciences (CPIS) of Sokendai. This work was supported by JSPS KAKENHI Grants No. 18K03700, No. 18H04444, No. 18H01212 and No. 19K23443.

REFERENCES

- Aloy M. A., Ibáñez J. M., Martí J. M., Gómez J.-L., Müller E., 1999, *ApJL*, **523**, L125
- Aloy M. A., Müller E., Ibáñez J. M., Martí J. M., MacFadyen A., 2000, *ApJL*, **531**, L119
- Aloy M.-Á., Martí J.-M., Gómez J.-L., Agudo I., Müller E., Ibáñez J.-M., 2003, *ApJL*, **585**, L109
- Aloy M. A., Janka H.-T., Müller E., 2005, *A&A*, **436**, 273
- Asano K., Hayashida M., 2015, *ApJL*, **808**, L18
- Asano K., Hayashida M., 2018, *ApJ*, **861**, 31
- Asano K., Terasawa T., 2015, *MNRAS*, **454**, 2242
- Baum S. A., et al., 1997, *ApJ*, **483**, 178
- Begelman M. C., 1998, *ApJ*, **493**, 291
- Begelman M. C., Cioffi D. F., 1989, *ApJL*, **345**, L21
- Blandford R. D., Pringle J. E., 1976, *MNRAS*, **176**, 443
- Bromberg O., Tchekhovskoy A., 2016, *MNRAS*, **456**, 1739
- Bromberg O., Nakar E., Piran T., Sari R., 2011, *ApJ*, **740**, 100
- Bromberg O., Granot J., Lyubarsky Y., Piran T., 2014, *MNRAS*, **443**, 1532
- Chandrasekhar S., 1961, Hydrodynamic and hydromagnetic stability
- Daly R. A., Marscher A. P., 1988, *ApJ*, **334**, 539
- Eichler D., 1993, *ApJ*, **419**, 111
- Fanaroff B. L., Riley J. M., 1974, *MNRAS*, **167**, 31P
- Ferrari A., Trussoni E., Zaninetti L., 1978, *A&A*, **64**, 43
- Ghosh S., Foyi H., Friedrich R., 2010, *Journal of Fluid Mechanics*, **648**, 155
- Gómez J. L., Martí J. M., Marscher A. P., Ibáñez J. M., Alberdi A., 1997, *ApJL*, **482**, L33
- Gottlieb O., Nakar E., Piran T., 2018a, *MNRAS*, **473**, 576
- Gottlieb O., Nakar E., Piran T., Hotokezaka K., 2018b, *MNRAS*, **479**, 588
- Gottlieb O., Levinson A., Nakar E., 2019, *MNRAS*, **488**, 1416
- Gourgouliatos K. N., Komissarov S. S., 2018a, *Nature Astronomy*, **2**, 167
- Gourgouliatos K. N., Komissarov S. S., 2018b, *MNRAS*, **475**, L125
- Hardee P. E., 1979, *ApJ*, **234**, 47
- Hardee P. E., Rosen A., Hughes P. A., Duncan G. C., 1998, *ApJ*, **500**, 599
- Hardee P. E., Hughes P. A., Rosen A., Gomez E. A., 2001, *ApJ*, **555**, 744
- Hillier A. S., 2016, *MNRAS*, **462**, G256
- Hughes P. A., Miller M. A., Duncan G. C., 2002, *ApJ*, **572**, 713
- Ito H., Matsumoto J., Nagataki S., Warren D. C., Barkov M. V., 2015, *ApJL*, **814**, L29
- Ito H., Matsumoto J., Nagataki S., Warren D. C., Barkov M. V., Yonetoku D., 2019, *Nature Communications*, **10**, 1504
- Just O., Obergaulinger M., Janka H.-T., Bauswein A., Schwarz N., 2016, *ApJL*, **816**, L30
- Komissarov S. S., 1999, *MNRAS*, **308**, 1069
- Komissarov S. S., Falle S. A. E. G., 1997, *MNRAS*, **288**, 833
- Komissarov S. S., Falle S. A. E. G., 1998, *MNRAS*, **297**, 1087
- Komissarov S. S., Gourgouliatos K. N., Matsumoto J., 2019, *MNRAS*, **488**, 4061
- Konigl A., 1980, *Physics of Fluids*, **23**, 1083
- Laing R. A., Bridle A. H., 2014, *MNRAS*, **437**, 3405
- Lazzati D., Morsony B. J., Begelman M. C., 2009, *ApJL*, **700**, L47
- Leismann T., Antón L., Aloy M. A., Müller E., Martí J. M., Miralles J. A., Ibáñez J. M., 2005, *A&A*, **436**, 503
- Li Y., Wiita P. J., Schuh T., Elghossain G., Hu S., 2018, *ApJ*, **869**, 32
- López-Cámara D., Morsony B. J., Begelman M. C., Lazzati D., 2013, *ApJ*, **767**, 19
- Lundquist S., 1951, *Physical Review*, **83**, 307
- Martí J. M., Müller E., Font J. A., Ibáñez J. M. Z., Marquina A., 1997, *ApJ*, **479**, 151
- Martí J. M., Perucho M., Gómez J. L., 2016, *ApJ*, **831**, 163
- Matsumoto J., Masada Y., 2013, *ApJL*, **772**, L1
- Matsumoto J., Masada Y., Shibata K., 2012, *ApJ*, **751**, 140
- Matsumoto J., Aloy M. A., Perucho M., 2017, *MNRAS*, **472**, 1421
- Meliani Z., Keppens R., 2007, *A&A*, **475**, 785
- Meliani Z., Keppens R., 2009, *ApJ*, **705**, 1594
- Meliani Z., Keppens R., Giacomazzo B., 2008, *A&A*, **491**, 321
- Mignone A., Bodo G., 2005, *MNRAS*, **364**, 126
- Mignone A., McKinney J. C., 2007, *MNRAS*, **378**, 1118
- Millas D., Keppens R., Meliani Z., 2017, *MNRAS*, **470**, 592
- Mimica P., Aloy M.-A., Agudo I., Martí J. M., Gómez J. L., Miralles J. A., 2009, *ApJ*, **696**, 1142
- Mizuno Y., Hardee P., Nishikawa K.-I., 2007, *ApJ*, **662**, 835
- Mizuno Y., Lyubarsky Y., Nishikawa K.-I., Hardee P. E., 2009, *ApJ*, **700**, 684
- Mizuno Y., Gómez J. L., Nishikawa K.-I., Meli A., Hardee P. E., Rezzolla L., 2015, *ApJ*, **809**, 38
- Mizuta A., Ioka K., 2013, *ApJ*, **777**, 162
- Mizuta A., Yamada S., Takabe H., 2004, *ApJ*, **606**, 804
- Mizuta A., Yamasaki T., Nagataki S., Mineshige S., 2006, *ApJ*, **651**, 960
- Mizuta A., Kino M., Nagakura H., 2010, *ApJL*, **709**, L83
- Mohseni K., Colonius T., 2000, *Journal of Computational Physics*, **157**, 787
- Morsony B. J., Lazzati D., Begelman M. C., 2007, *ApJ*, **665**, 569
- Murguía-Berthier A., Montes G., Ramirez-Ruiz E., De Colle F., Lee W. H., 2014, *ApJL*, **788**, L8
- Nagakura H., Ito H., Kiuchi K., Yamada S., 2011, *ApJ*, **731**, 80
- Nagakura H., Hotokezaka K., Sekiguchi Y., Shibata M., Ioka K., 2014, *ApJL*, **784**, L28
- Nishihara K., Wouchuk J. G., Matsuoka C., Ishizaki R., Zhakhovsky V. V., 2010, *Philosophical Transactions of the Royal Society of London Series A*, **368**, 1769
- Payne D. G., Cohn H., 1985, *ApJ*, **291**, 655
- Perucho M., Martí J. M., 2007, *MNRAS*, **382**, 526
- Perucho M., Hanzsz M., Martí J. M., Sol H., 2004, *A&A*, **427**, 415
- Perucho M., Martí J. M., Hanzsz M., 2005, *A&A*, **443**, 863
- Perucho M., Hanzsz M., Martí J.-M., Miralles J.-A., 2007, *Phys. Rev. E*, **75**, 056312
- Perucho M., Martí J. M., Cela J. M., Hanzsz M., de La Cruz R., Rubio F., 2010, *A&A*, **519**, A41
- Perucho M., Quilis V., Martí J.-M., 2011, *ApJ*, **743**, 42
- Perucho M., Martí J.-M., Quilis V., Ricciardelli E., 2014, *MNRAS*, **445**, 1462
- Perucho M., Martí J.-M., Quilis V., Borja-Lloret M., 2017, *MNRAS*, **471**, L120
- Perucho M., Martí J.-M., Quilis V., 2019, *MNRAS*, **482**, 3718
- Porth O., Komissarov S. S., 2015, *MNRAS*, **452**, 1089
- Rossi P., Mignone A., Bodo G., Massaglia S., Ferrari A., 2008, *A&A*, **488**, 795
- Sanders R. H., 1983, *ApJ*, **266**, 73

- Scheck L., Aloy M. A., Martí J. M., Gómez J. L., Müller E., 2002, *MNRAS*, **331**, 615
- Spruit H. C., Foglizzo T., Stehle R., 1997, *MNRAS*, **288**, 333
- Toma K., Komissarov S. S., Porth O., 2017, *MNRAS*, **472**, 1253
- Turland B. D., Scheuer P. A. G., 1976, *MNRAS*, **176**, 421
- Walg S., Achterberg A., Markoff S., Keppens R., Meliani Z., 2013, *MNRAS*, **433**, 1453
- Zhang W., Woosley S. E., MacFadyen A. I., 2003, *ApJ*, **586**, 356
- Zhang W., Woosley S. E., Heger A., 2004, *ApJ*, **608**, 365

APPENDIX A: RESOLUTION STUDY IN GROWTH OF OSCILLATION-INDUCED INSTABILITIES IN MODEL H+

The influence of the numerical resolution on the stability of the jet is investigated by changing the grid spacing for one particular simulation model. For this purpose, the model H+ is chosen as a reference because the evolving finger-like structure, which is one of the typical features of the oscillation-induced instabilities, is the most remarkable in this model compared with the others (i.e. H-, C+ and C-).

The simulation setup of model H+ was described in Section 3.1. The resolution of the fiducial run is $(N_r, N_\phi, N_z) = (150, 160, 3000)$. We run 6 additional models only with changing the grid spacing and compare them with the fiducial one. The number of grid points in each direction is summarized for each model in table A1. The direction in which we change the resolution is distinguished by the labels “r”, “ ϕ ” and “z” in the model name. The label containing “high (low)” is corresponding to the model with the twice (half) of the directional resolution adopted in the fiducial one.

The upper panels of Fig. A1 are the distributions of $\gamma^2 \rho h'$ on the cutting plane along the z -axis at $t = 850$ for the models with different resolutions. In all the models, $\gamma^2 \rho h'$ of the jet is larger than that of cocoon at the jet interface, indicating that the onset condition for the oscillation-induced RTI is satisfied. As a result of it, we can find that the jet is deformed in all the models regardless of the number of grid points. Shown in the lower panels of Fig. A1 is the distribution of the passive tracer, f , on the x - y cutting plane at $z = 100$ when $t = 850$ for each model. We can find that the finger-like structure is excited and evolved regardless of the number of the grid points in all the models, while the typical azimuthal wavelength of it is different between models and seems to be corresponding to ~ 10 numeric cells for each model. This implies that, the higher the numerical resolution, the more the jet is destabilized by shorter wavelength modes with higher growth rate.

As a conclusion, overall results of our resolution study indicate that the grid spacing adopted in our simulation study is enough, at least, to discuss the stability of the jet qualitatively. However, it may be necessary to use much more numerical grids to study “quantitatively” the magnitudes of the mixing, transport, and their impacts on the jet propagation dynamics at the nonlinear stage.

Table A1. Number of grid points in each model for the resolution study.

Model	N_r	N_ϕ	N_z
H+	150	160	3000
r-low	75	160	3000
ϕ -low	150	80	3000
z-low	150	160	1500
r-high	300	160	3000
ϕ -high	150	320	3000
z-high	150	160	6000

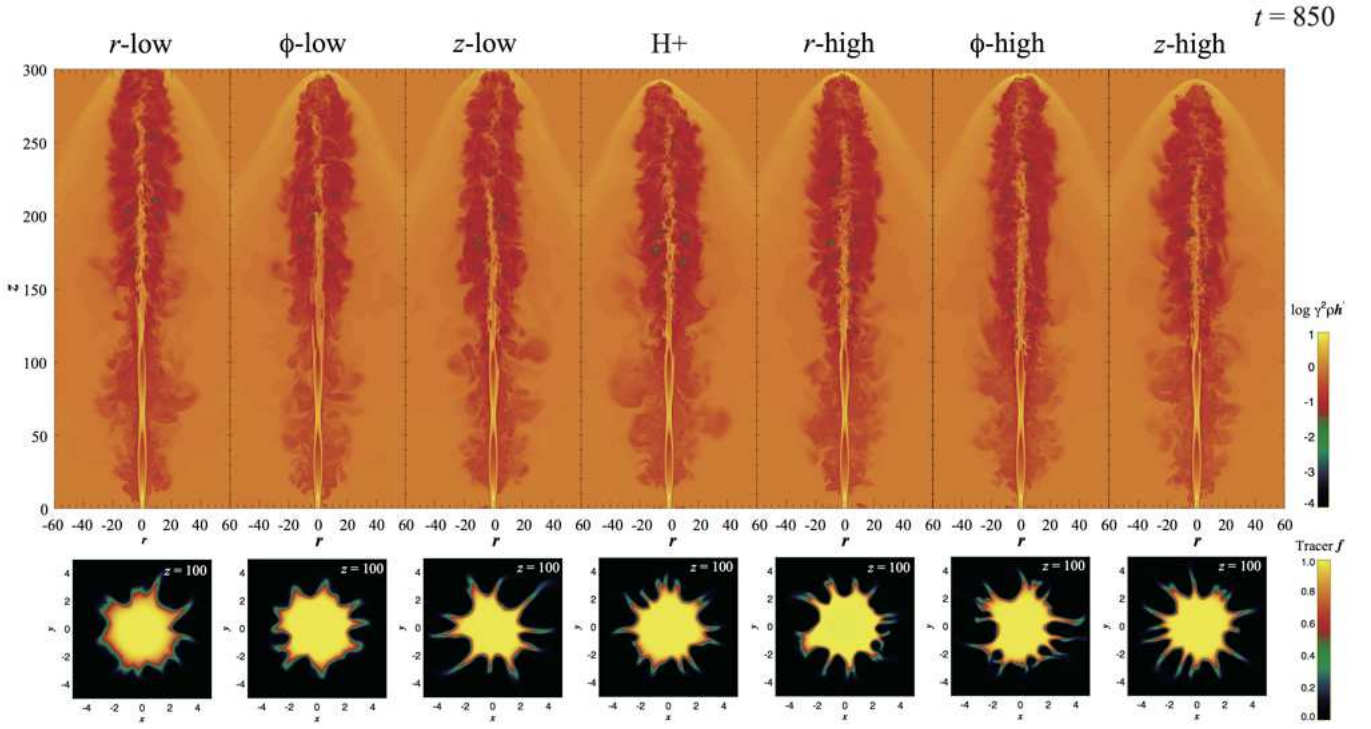


Figure A1. Upper panels: Spatial distribution of $\gamma^2 \rho h'$ on the cutting plane along the z -axis at $t = 850$. Lower panels: 2D cut of the passive tracer in the x - y plane at $z = 100$ when $t = 850$.